

The role of OCO-3 XCO₂ retrievals in estimating global terrestrial net ecosystem exchanges

Xingyu Wang¹, Fei Jiang^{1,2,5,*}, Hengmao Wang¹, Zhengqi Zhang¹, Mousong Wu¹, Jun Wang¹, Wei He⁴, Weimin Ju^{1,5}, Jing M. Chen^{3,6}

¹Jiangsu Provincial Key Laboratory of Geographic Information Science and Technology, International Institute for Earth System Science, Nanjing University, Nanjing, 210023, China.

²Jiangsu Center for Collaborative Innovation in Geographical Information Resource Development and Application, Nanjing, 210023, China.

³Department of Geography and Planning, University of Toronto, Toronto, Ontario M5S3G3, Canada.

⁴Zhejiang Carbon Neutral Innovation Institute, Zhejiang University of Technology, Hangzhou, Zhejiang 310014, China.

⁵Frontiers Science Center for Critical Earth Material Cycling, Nanjing University, Nanjing, 210023, China.

⁶School of Geographical Sciences, Fujian Normal University, Fuzhou, 350007, China

***Corresponding author: Fei Jiang (jiangf@nju.edu.cn)**

24 **Abstract**

25 Satellite-based column-averaged dry air CO₂ mole fraction (XCO₂) retrievals are frequently used to
26 improve the estimates of terrestrial net carbon exchanges (NEE). The Orbiting Carbon Observatory 3
27 (OCO-3) satellite, launched in May 2019, was designed to address important questions about the dis-
28 tribution of carbon fluxes on Earth, but its role in estimating global terrestrial NEE remains unclear.
29 Here, using the Global Carbon Assimilation System, version 2, we investigate the impact of OCO-3
30 XCO₂ on the estimation of global NEE by assimilating the OCO-3 XCO₂ retrievals alone and in com-
31 bination with the OCO-2 XCO₂ retrievals. The results show that when only the OCO-3 XCO₂ is as-
32 similated (Exp_OCO3), the estimated global land sink is significantly lower than that from the OCO-
33 2 experiment (Exp_OCO2). The estimate from the joint assimilation of OCO-3 and OCO-2
34 (Exp_OCO3&2) is comparable on a global scale to that of Exp_OCO2. However, there are significant
35 regional differences. Compared to the observed global annual CO₂ growth rate, Exp_OCO3 has the
36 largest bias, and Exp_OCO3&2 shows the best performance. Furthermore, validation with independent
37 CO₂ observations shows that the biases of the Exp_OCO3 are significantly larger than those of
38 Exp_OCO2 and Exp_OCO3&2 at mid and high latitudes. The reasons for the poor performance of
39 assimilating OCO-3 XCO₂ alone include the lack of observations beyond 52°S and 52°N, the large
40 fluctuations in the data amount, and its varied observation time. probably due to the fact that OCO-3
41 only has observations from 52°S to 52°N. Our study indicates that assimilating OCO-3 XCO₂ retrievals
42 alone leads to an underestimation of land sinks at high latitudes, and that a joint assimilation of OCO-
43 2 XCO₂ and the OCO-3 XCO₂ retrievals observed in the afternoon is required for a better estimation
44 of global terrestrial NEE.

45
46
47
48
49
50
51

52 **1 Introduction**

53 The rising of the carbon dioxide (CO₂) concentration in the Earth's atmosphere in recent decades,
54 which is mainly caused by human activities, such as the burning of fossil fuels, deforestation and land-
55 use change, has become a global concern (Hansen et al., 2013). Terrestrial ecosystems and oceans
56 together absorb about 56 ~~per-cent~~^{0%} of anthropogenic CO₂ emissions (Friedlingstein et al., 2023).
57 Among them, terrestrial ecosystems play a crucial role in regulating the atmospheric CO₂ concentra-
58 tion. However, the carbon uptake capacity of terrestrial ecosystems varies considerably globally and
59 regionally (Bousquet et al., 2000; Takahashi et al., 2009; Piao et al., 2020). Therefore, accurate quanti-
60 fication of global and regional terrestrial net ecosystem exchange (NEE) is very important to under-
61 stand their role and potential in regulating changes in the atmospheric CO₂ concentration.

62 Atmospheric inversion is a major method for estimating surface carbon fluxes from observations
63 of atmospheric CO₂ concentration (Enting and Newsam, 1990; Gurney et al., 2002; Thompson et al.,
64 2016; Jiang et al., 2021), but it is more effective at the global scale than at the regional scale. A large
65 number of previous studies have shown that different atmospheric inversion models can produce rela-
66 tively consistent global estimates of carbon fluxes, but their performance at regional scales is variable.
67 In regions such as the tropics, southern hemisphere oceans, and most continental interiors (South
68 America, Africa and boreal Asia), the reliability of atmospheric inversions varies considerably due to
69 the heterogeneous distribution of *in-situ* observations, leading to an increase in the uncertainty of car-
70 bon flux estimates (Peylin et al., 2013; Wang et al., 2019). The use of satellite observations to constrain
71 atmospheric inversions can be effective in improving carbon flux estimates because of their better
72 spatial coverage (Basu et al., 2013; Byrne et al., 2020; Jiang et al., 2021; Wang et al., 2022; He et al.,
73 2023a). The National Aeronautics and Space Administration (NASA) launched the Orbiting Carbon
74 Observatory 2 (OCO-2) satellite in 2014 (Crisp et al., 2017; Eldering et al., 2012, 2017), followed by
75 the Orbiting Carbon Observatory 3 (OCO-3) satellite in 2019 (Taylor et al., 2023). The OCO-~~2~~ satel-
76 lites have a high sensitivity to column-averaged dry air CO₂ mole fraction (XCO₂), a fine footprint,
77 and a good spatial coverage, and can therefore be used to better constrain surface carbon flux estimates.
78 In previous studies, many atmospheric inversion models have used the XCO₂ from the OCO-2 satel-
79 lites to estimate global (e.g., Crowell et al., 2019; Peiro et al., 2022; Byrne et al., 2023) and regional

80 (e.g., Palmer et al., 2019; Byrne et al., 2021; Philip et al., 2022; He et al., 2022; He et al., 2023a)
81 surface carbon fluxes. For example, Miller et al. (2018) evaluated the effectiveness of OCO-2 obser-
82 vations in constraining regional biospheric CO₂ fluxes. Their findings indicate that OCO-2 observa-
83 tions are most effective at continental and hemispheric scales. Byrne et al. (2022) utilised OCO-2 data
84 to fill a gap in station observations at high latitudes. Their study confirmed the presence of significant
85 and widely distributed early cold-season CO₂ emissions in the northeastern region of Eurasia. Further-
86 more, several studies have utilised OCO-2 XCO₂ data to investigate the impact of climate extremes on
87 terrestrial NEE, such as El Niño (e.g., Liu et al., 2017) and droughts (He et al., 2023 b; Chen et al.,
88 2024). OCO-3 introduces new technologies and observational methods to monitor CO₂ on Earth, of-
89 fering the same ~~temporal and~~ spatial resolution as OCO-2. It is aimed at detecting mid-latitude regions
90 where human CO₂ emissions are concentrated. However, few studies have used the OCO-3 XCO₂
91 retrievals to constrain global and regional surface carbon fluxes ~~til~~until now. Therefore, it is important
92 to investigate the impact of assimilating OCO-3 observations on the estimates of global and terrestrial
93 carbon sinks.

94 In this study, we used both OCO-2 and OCO-3 XCO₂ retrievals to invert global and regional
95 carbon fluxes for the period of 2020-2022 with the Global Carbon Assimilation System, version 2
96 (GCASv2) (Jiang et al., 2021). The XCO₂ retrievals from OCO-2 and OCO-3 were assimilated sepa-
97 rately and together in order to disentangle the effect of OCO-3 XCO₂ retrievals on the estimates of
98 global and regional terrestrial carbon sinks.

99

100 **2 Methods and data**

101 **2.1 Inversion method**

102 The Global Carbon Assimilation System, version 2 (GCASv2) (Jiang et al., 2021; Wang et al.,
103 2021) designed primarily for assimilating satellite XCO₂ retrievals was adopted in this study to invert
104 surface carbon fluxes. The system uses the Model for Ozone and Related Chemical Tracers, version 4
105 (MOZART-4; Emmons et al., 2010) to simulate three-dimensional atmospheric CO₂ concentrations,
106 and an ensemble square root filter (EnSRF; Whitaker and Hamill, 2002) to implement the inversion of
107 surface fluxes. MOZART-4 is an offline global chemical transport model developed in the National

Center for Atmospheric Research (NCAR). It can be driven by essentially any meteorological data set and with any emissions inventory, so there is not a unique standard simulation (Emmons et al., 2010). We turned off all gas-phase, heterogeneous chemical reactions, aerosol and deposition processes in the MOZART4 model and added a corresponding number of CO₂ tracers according to the ensemble number in GCASv2, in order to allow the model to run more quickly. EnSRF assimilates observations in a sequential way, and obviates the need to perturb the observations. It shows good performance as long as the observation errors are uncorrelated (Houtekamer and Mitchell, 2001). GCASv2 is an upgrade from the GCAS (Zhang et al., 2015) that was established in 2015. The main upgrades include: 1) the addition of an assimilation module for satellite observations; 2) a change in the assimilation algorithm (i.e., EnSRF); 3) a change in the operational flow of the assimilation system; 4) the addition of a ‘super-observation’ scheme; 5) inversion of fluxes at the grid scale; and 6) an improvement in the localization scheme.

GCASv2 runs cyclically, with a two-step optimization strategy in each assimilation window (1 week). In the first step, the prior fluxes (X_0^b) in each grid are independently perturbed with a random number (δ_i) drawn from a Gaussian distribution with mean of 0 and standard deviation of 1, and a scaling factor (λ) that represents the uncertainty of each prior flux (Eq. 1).

$$X_i^b = X_0^b + \lambda \times \delta_i \times X_0^b, i = 1, 2, \dots, N \quad (1)$$

Then, the perturbed fluxes are put into the MOZART-4 model to simulate ensembles of CO₂ concentrations. The CO₂ profiles are sampled according to the locations and times of XCO₂ observations and converted to the simulated ensembles of XCO₂ ($XCO_{2,i}^m$) according to prior XCO₂ (XCO_2^a), prior XCO₂ profiles ($y_{a,j}$), pressure weighting function (h_j), and averaging kernel (a_j) of the XCO₂ retrievals (Eq. 2).

$$XCO_{2,i}^m = XCO_2^a + \sum_j h_j a_j (A(CO_{2,i}) - y_{a,j}) \quad (2)$$

Subsequently, the perturbed fluxes (X_i^b), the simulated XCO₂ ensembles and the observed XCO₂ (y) are used in EnSRF to optimize the carbon fluxes (\bar{X}^a) by assimilating the observations (Eqs. 3-5). The background error covariance matrix (P^b) is calculated based on X_i^b according to Eq. (3), where \bar{X}^b is the mean of X_i^b . The posterior flux (\bar{X}^a) is a correction to the prior flux using the bias between

135 simulated and observed XCO₂ ($y - H\bar{X}^b$) and the Kalman gain matrix (K) (Eq. 4). And K is calculated
 136 according to Eq. (5), which is a function of model-data mismatch error covariance matrix (R) and the
 137 background error covariance matrix.

$$138 \quad P^b = \frac{1}{n-1} \sum_{i=1}^n (X_i^b - \bar{X}^b) (X_i^b - \bar{X}^b)^T \quad (3)$$

$$139 \quad \bar{X}^a = \bar{X}^b + K(y - H\bar{X}^b) \quad (4)$$

$$140 \quad K = P^b H^T (H P^b H^T + R)^{-1} \quad (5)$$

141 ~~In and~~ the second step, ~~is to input~~ the optimized carbon fluxes are put into the MOZART-4
 142 model to obtain the initial field of the next assimilation window. This scheme allows compensation of
 143 inversion results between neighboring windows and mass conservation between flux adjustments and
 144 concentration changes.

145 In order to reduce the effects of horizontal observation error correlation and representativeness
 146 error, based on the optimal estimation theory (Miyazaki et al., 2012), the system also performs a “su-
 147 per-observation” scheme, which combines multiple observations located within a same model grid into
 148 a single high-precision “super-observation”. In this method, it first calculates the simulated XCO₂ cor-
 149 responding to each observed XCO₂ based on the observation time and location, and then, it performs
 150 a retrieval error-weighted average for all the simulated and observed XCO₂ falling within the same
 151 model grid in the DA window, respectively.

152 There are inevitably spurious correlations in the EnKF method, to reduce the effect of spurious
 153 correlations, a two-layers localization scale was adopted in GCASv2, which is used to select which
 154 observations in a grid to can be used for the flux analysis for each grid. The localization technique is
 155 based on the correlation coefficient between the simulated XCO₂ ensembles ($XCO_{2,i}^m$) in each observa-
 156 tion location and the perturbed fluxes (X_i^b) in current model grids and their distances. The observations
 157 will be accepted for assimilation if the distance is less than 500 km and the correlation coefficient is
 158 greater than 0; and if the distance is greater than or equal to 500 km and less than 3000 km and the
 159 correlation coefficient should be significant ($p < 0.05$). Otherwise, the observations are not accepted.
 160 The reason for this scheme is that considering the atmospheric horizontal diffusion, we believe that

161 there must be a correlation between the flux of one grid and the concentrations in its neighbouring
162 grids, and therefore observations are accepted as long as this correlation coefficient is greater than zero.
163 In contrast, at distant locations (>500 km), where the effect of atmospheric horizontal diffusion is
164 essentially negligible, the relationship between source and receptor is mainly due to atmospheric
165 transport, and in order to minimize spurious correlations we require that such correlations must be
166 significant. More details of the system can be found in Jiang et al (2021).

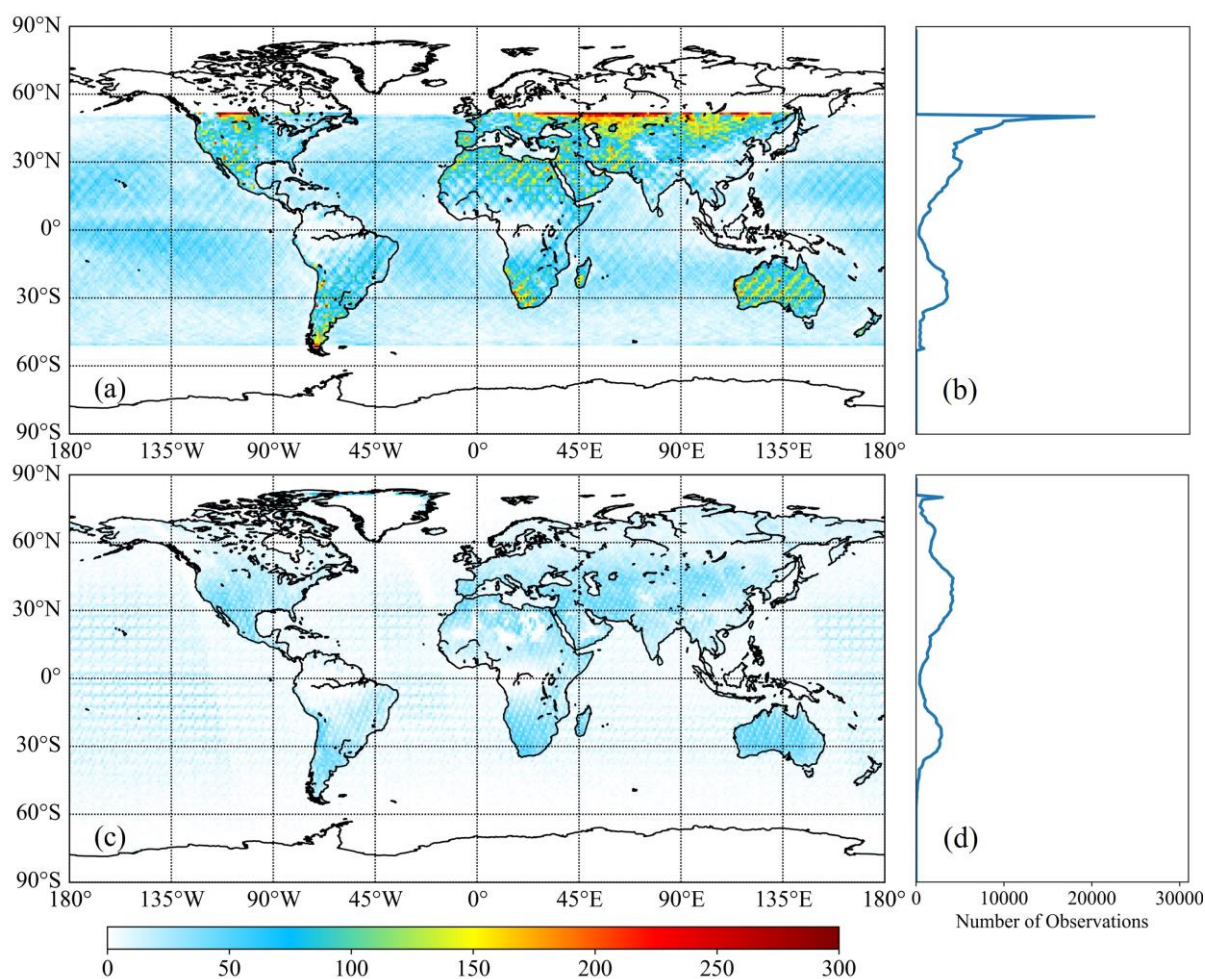
167 2.2 OCO-2 and OCO-3 XCO₂ retrievals

168 In July 2014, the Orbiting Carbon Observatory (OCO) -2 satellite was launched by NASA with
169 the primary objective of providing accurate space-based measurements to quantify changes in XCO₂.
170 The satellite is equipped with three high-resolution spectrometers that can detect two near-infrared
171 wavelength bands (1.61 μm and 2.06 μm) of sunlight reflectance spectra to observe CO₂. In May 2019,
172 NASA launched OCO-3 to the International Space Station (ISS) to detect CO₂ in mid-latitudes, where
173 human emissions are more concentrated. OCO-3 operates in a low-inclination orbit from 52°S to 52°N
174 and is equipped with three high-resolution spectrometers, providing the same ~~temporal and~~ spatial
175 resolutions and similar observation mode as the OCO-2 satellites (Taylor et al., 2023). However, since
176 OCO-3 is mounted on the ISS, its observation time and frequency for the same place is different from
177 the OCO-2. The detection target is also essentially the same.

178 The XCO₂ data from OCO-3 and OCO-2 used in this study are bias-corrected products from
179 August 2019 to December 2022 at the image element level. The data are sourced from Version 10.4r
180 Level 2 Lite and Version 11.1r Level 2 Lite, respectively. Before using them in our inversion system,
181 it is essential to pre-process the data. First, both the land (Land Nadir + Land Glint, LNLG) and ocean
182 (Ocean Glint, OG) retrievals were adopted, and they were filtered using the parameter of XCO₂_qual-
183 ity_flag, which indicates the quality of the data. Only data with XCO₂_quality_flag=0 was selected for
184 assimilation in this study. Then, the LNLG and OG retrievals and their corresponding retrieval param-
185 eters (namely XCO_2^a , $\gamma_{a,j}$, h_j , and a_j in Eq. 2) were re-gridded to a spatial resolution of 1° × 1° and
186 5° × 5° using the arithmetic averaging method, respectively. For the OG data, we used a coarser re-
187 gridding resolution, that is because the distribution of XCO₂ is more homogeneous on sea than on land.
188 Finally, both OCO-3 and OCO-2 XCO₂ retrievals were converted to the X2019 scale of the World

189 Meteorological Organization (WMO) following Hall et al., (2021). Figure 1a and c display the distri-
190 bution and coverage of screened OCO-3 and OCO-2 XCO₂ retrievals from 2020 to 2022. Compared
191 to OCO-2, OCO-3 has more observational data in the mid-latitudes of the northern and southern hem-
192 ispheres, especially in arid and semi-arid regions.

193 Following Jiang et al. (2022), the model-data mismatch errors were amplified by a factor on top
194 of the XCO₂ posterior errors, but with the minimum observation error setting to 1 ppm. It needs to be
195 noted that in the OCO-3 and OCO-2 products, the XCO₂ posterior errors of OG retrievals (0.48 ± 0.11
196 and 0.51 ± 0.15 ppm in 2020 for OCO-2 and OCO-3, respectively) are smaller than LNLG (0.54 ± 0.12
197 and 0.64 ± 0.18 ppm in 2020 for OCO-2 and OCO-3, respectively), but in fact, the observational error
198 should be greater at sea than on land (Peiro et al., 2022). Therefore, before multiplying by a uniform
199 factor, we increased the XCO₂ posterior errors of OG retrievals by 0.2 ppm. Taylor et al. (2023) re-
200 ported that the mean of the uncertainties for the OCO-2 and OCO-3 quality-filtered and bias-corrected
201 XCO₂ are 1.0 and 1.3 ppm, respectively. Considering that the global atmospheric transport model may
202 have an uncertainty of about 1.0 ppm (Lauvaux et al., 2009), thus in this study, we set the amplification
203 factor to be 3.5. Through this treatment, the mean model-data mismatch errors of LNLG and OG are
204 about 1.9 and 2.4 ppm for OCO-2, and 2.3 and 2.5 ppm for OCO-3, respectively.



205

206 **Figure1.** Data amount (the sum of 2020-2022) of XCO₂ in each grid cell (1° × 1°) and at each latitude used
 207 in this study (a, b, OCO-3; c, d, OCO-2)

208

2.3 Prior carbon fluxes

209

210

211

212

213

214

215

216

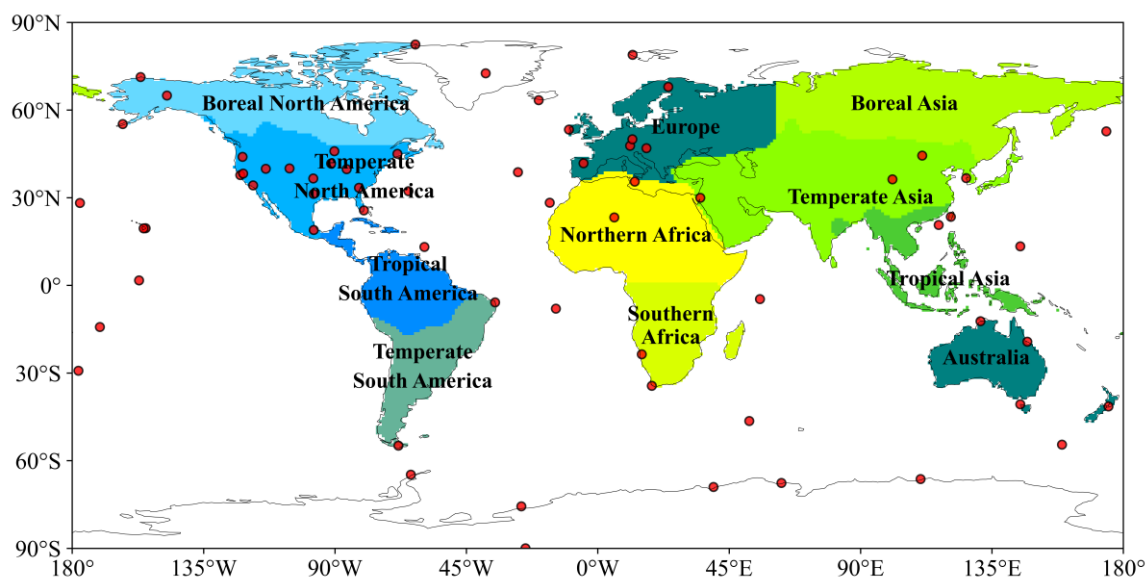
217

There are 4 prior carbon fluxes used in this study, which are terrestrial NEE, ocean-atmosphere (OCN) carbon exchanges, fossil fuel and cement production (FOSSIL) carbon emissions, and biomass combustion (FIRE) carbon emissions. The NEE were simulated using the BEPS model (Chen et al., 2019). The OCN fluxes were derived from the mean of the JMA Ocean CO₂ Map (Iida et al., 2021), which contains a global product with 1°×1° resolution (Globe, v2022) and another product for the Northwest Pacific region with a resolution of 0.25°×0.25° (The western North Pacific, v2023). These two products were integrated before they are used in this study. The FOSSIL carbon emissions were obtained from GCP-GridFEDv2023.1 (Jones et al., 2021), which contains monthly global carbon emissions from fossil fuels, cement production, and cement product weathering carbon sequestration at a

218 spatial resolution of $0.1^{\circ} \times 0.1^{\circ}$. The FIRE carbon emissions were obtained directly from the Global
219 Fire Emissions Database, Version 4.1 (GFED4.1s; Randerson et al., 2017). All 4 prior fluxes cover the
220 entire time period of this study (i.e., August 2019 to December 2022) and they were re-gridded to a
221 unified spatial resolution of $1^{\circ} \times 1^{\circ}$ before used in the GCASv2 system.

222 2.4 Evaluation data and methods

223 Due to the significant spatial scale discrepancy between the inverted fluxes and the *in-situ* ob-
224 served fluxes, direct validation of the posterior Net Ecosystem Exchange (NEE) using observed data
225 is typically unattainable. However, we are able to indirectly evaluate the posterior fluxes by comparing
226 the atmospheric CO_2 concentrations, simulated with the posterior fluxes, against independent CO_2
227 measurements. (e.g., Jin et al., 2018; Wang et al., 2019; Feng et al., 2020; Jiang et al., 2021). In this
228 study, we used surface flask observations at 66 sites from the ObsPack dataset (ObsPack v9.1, Schuldt
229 et al., 2023) to independently assess the posterior fluxes. The screening of the 66 sites followed the
230 methodology of Jiang et al. (2022). The distribution of the 66 flask sites is shown in Figure 2. The
231 specific metrics assessed were the statistics of mean bias (BIAS), absolute bias (MAE), and root mean
232 square error (RMSE). We calculated annual BIAS, MAE, and RMSE globally, for different latitudinal
233 zones, and for different land areas.



234
235 **Figure2.** Distributions of the observation sites used for independent evaluation in this study and the 11 Trans-
236 Com-3 regions on land defined in Botta et al. (2012).

237 **3 Inversion experiments**

238 The GCASv2 system was run from 1 August 2019 to 31 December 2022. The initial five months
239 were designated as the spin-up stage, and the results from January 2020 to December 2022 were ana-
240 lyzed in this study. Three inversion experiments were conducted: (1) assimilation of OCO-3 XCO₂ (all
241 inversion experiments use OG+LNLG data) retrievals alone (Exp_OCO3); (2) assimilation of OCO-2
242 XCO₂ retrievals alone (Exp_OCO2); and (3) simultaneous assimilation of OCO-3 and OCO-2 XCO₂
243 retrievals (Exp_OCO3&2). In each experiment, the methodology employed was consistent with that
244 of previous studies (Peters et al., 2007; Jiang et al., 2021, 2022), only the NEE and OCN fluxes were
245 optimized, and the FIRE and FOSSIL emissions are prescribed. According to Eq. (1), the prior NEE
246 and OCN fluxes were perturbed using Eq. (6).

$$247 \quad X_i^b = \lambda_{NEE} \times \delta_{i,NEE} \times X_{NEE}^b + \lambda_{ocn} \times \delta_{i,ocn} \times X_{OCN}^b + X_{Fire}^b + X_{Fossil}^b, i = 1, 2, \dots, N \quad (6)$$

248 where X_{NEE}^b , X_{OCN}^b , X_{Fire}^b , and X_{Fossil}^b represent the prior fluxes of NEE, OCN, FIRE, and FOSSIL,
249 respectively; δ_i is random perturbation samples, which is independent between grids; λ_{NEE} and
250 λ_{ocn} are the scaling factors for prior NEE and OCN fluxes, which were set to be 6 and 10 in this study,
251 respectively. As described above, the prior fluxes have a spatial resolution of $1^\circ \times 1^\circ$, for $\delta_{i,NEE}$ and
252 $\delta_{i,ocn}$, we adopted a spatial resolution of $3^\circ \times 3^\circ$, and the outputs of the posterior fluxes have the same
253 spatial resolution with the prior fluxes, that means in each $3^\circ \times 3^\circ$ grid, the prior fluxes were adjusted
254 with a same factor.

255 Additionally, two forward simulations were conducted to obtain the prior and posterior CO₂ con-
256 centrations, which were then compared with the independent CO₂ observations to assess the posterior
257 carbon fluxes. Following Jiang et al. (2022), MOZART-4 is driven by the $1.9^\circ \times 2.5^\circ$ grids version of
258 the GEOS5 Global Atmosphere Forcing Data (Tilmes, 2016). It has a vertical level of 72 layers, and
259 MOZART-4 uses the lowest 56 vertical levels of GEOS-5 and the same spatial resolution with GEOS-
260 5 data.

261 **4 Results and discussion**

262 **4.1 Global carbon budget**

263 Table 1 presents the prior and the posterior annual global carbon budgets from the 3 inversion

264 experiments during 2020-2022. The global terrestrial NEEs obtained from the Exp_OCO3,
 265 Exp_OCO2, and Exp_OCO3&2 experiments are -3.41 ± 0.65 , -4.17 ± 0.60 , and -4.14 ± 0.57 PgC yr⁻¹,
 266 respectively. The global NEE inferred from the Exp_OCO3 is significantly weaker than those from
 267 Exp_OCO2 and Exp_OCO3&2, and the latter two are comparable. For the OCN carbon sink,
 268 Exp_OCO3 has the strongest sink but is closest to the a priori result, while Exp_OCO2 and
 269 Exp_OCO3&2 have essentially the same sink. Combined with the FOSSIL and FIRE carbon emissions,
 270 the global net carbon fluxes are 4.74 ± 0.77 , 5.55 ± 0.67 , 4.90 ± 0.63 , and 4.93 ± 0.60 PgC yr⁻¹ for the a
 271 priori, Exp_OCO3, Exp_OCO2, and Exp_OCO3&2, respectively. In comparison with the average at-
 272 mospheric CO₂ growth rate of 4.936 PgC yr⁻¹ for 2020-2022 given by the Global Carbon Budget 2023
 273 (Friedlingstein et al., 2023), the results of Exp_OCO3&2 are the closest, with a mean bias of 0.03 PgC
 274 yr⁻¹, whereas Exp_OCO3 has the largest bias, with a deviation of 0.62 PgC yr⁻¹. This indicates that the
 275 carbon sinks in Exp_OCO3 may be significantly underestimated, and joint assimilation of OCO-2 and
 276 OCO-3 XCO₂ retrievals gives the best performance on a global scale.

277 **Table 1.** Global carbon budget estimated in the 3 inversion experiments (PgC yr⁻¹).

	Prior	Exp_OCO3	Exp_OCO2	Exp_OCO3&2
FOSSIL emissions			9.71	
FIRE emissions			1.97	
NEE	-4.10 ± 0.75	-3.41 ± 0.65	-4.17 ± 0.60	-4.14 ± 0.57
OCN fluxes	-2.84 ± 0.17	-2.71 ± 0.17	-2.61 ± 0.17	-2.61 ± 0.17
Global net carbon fluxes	4.74 ± 0.77	5.55 ± 0.67	4.90 ± 0.63	4.93 ± 0.60
Observed global CO ₂ growth rates			4.9693	

278

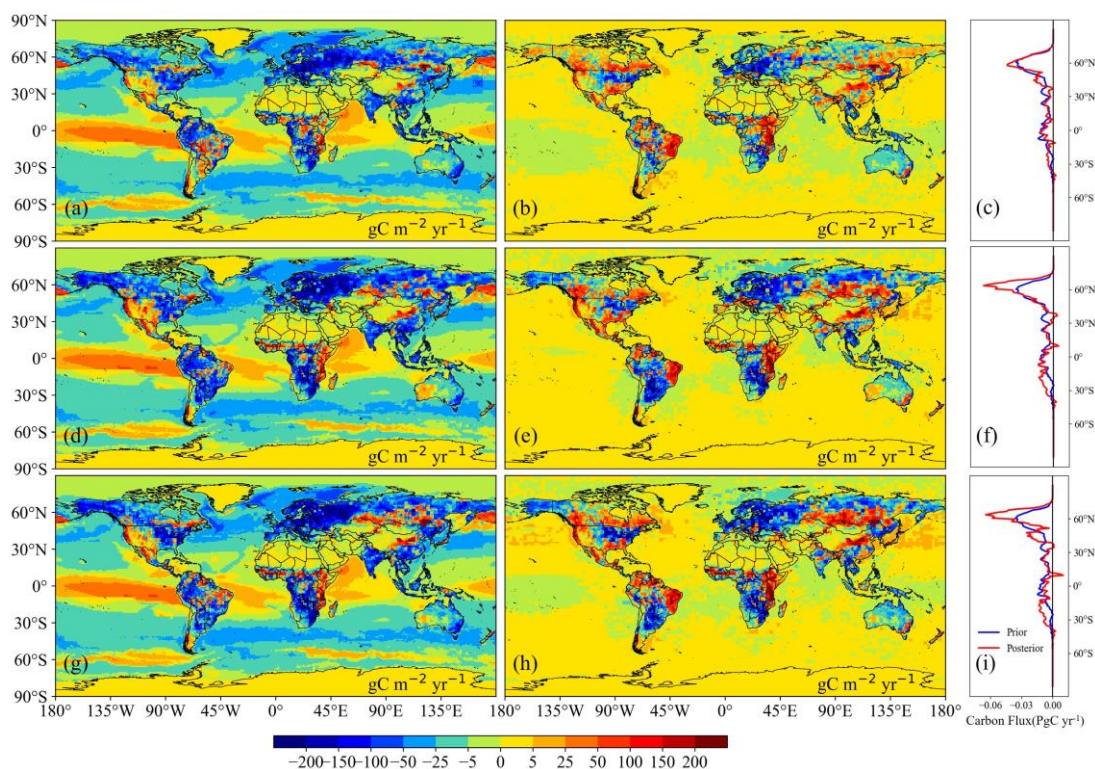
279 4.2 Regional NEE

280 Figure 3 shows the spatial distribution of annual mean posterior terrestrial fluxes and oceanic
 281 fluxes from the Exp_OCO3, Exp_OCO2, Exp_OCO3&2 and their differences against the a priori
 282 fluxes. Overall, the spatial distribution of carbon sources and sinks in terrestrial ecosystems obtained
 283 from different experiments is basically the same, with sinks in western North America (N.

284 America), eastern Amazonia, parts of Siberia, parts of Northwest China, central and western Australia,
285 and the Sahel region and eastern parts of Africa, while other areas are carbon sinks. However, the
286 carbon sources/sinks obtained from Exp_OCO3 exhibit a markedly different strength compared to
287 those derived from the other two experiments. Compared with the prior flux, the terrestrial carbon
288 sinks in northeastern China, most of Europe, northern Siberia, the central and northeastern United
289 States (US), and southern Africa increased significantly in all the 3 experiments. However, the increase
290 in terrestrial carbon sinks in regions other than northeastern China in the Exp_OCO2 and
291 Exp_OCO3&2 was greater than that in the Exp_OCO3. Meanwhile, in southern Canada, western and
292 southern US, eastern Brazil and northern South America (S. America), the Sahel region and eastern
293 parts of Africa, all the 3 inversion experiments show a significant decrease in the terrestrial carbon
294 sink. The degree of change in the inversion results is more pronounced in the Exp_OCO2 and
295 Exp_OCO3&2 than in the Exp_OCO3. Figure 3 also show the distribution of terrestrial carbon fluxes
296 along latitudes. The posterior and prior fluxes have a similar distribution trend along the latitude, with
297 a significant peak of carbon sink near 60°N, and the ~~peaks-strongest sinks~~ of Exp_OCO2 and
298 Exp_OCO3&2 are comparable, which are significantly ~~higher-stronger~~ than the a priori, while
299 Exp_OCO3 has the ~~weaker-lowest~~ peak of carbon sink and that is close to the a priori. In addition, it also
300 could be found that the terrestrial carbon sinks obtained from Exp_OCO3 are also significantly smaller
301 than those from Exp_OCO2 and Exp_OCO3&2 near 30°S.

302 In order to better understand and compare the differences among different inversion experiments,
303 we have aggregated the prior and the posterior NEEs into the 11 TransCom-3 land regions (Figure 2),
304 as shown in ~~Figure 4~~ Table 2. It is clearly that almost all terrestrial regions behave as carbon sinks, both
305 prior and posterior fluxes. Among the experiments, only the terrestrial NEE in northern Africa obtained
306 by Exp_OCO3&2 shows a weak carbon source. There is relatively good agreement between all the
307 inversion experiments on whether the land carbon flux is a source or sink, but there is significant
308 difference in the NEE values. In all regions except temperate N. America, northern Africa, temperate
309 Asia, and Australia, Exp_OCO3 shows a ~~weaker-lower~~ carbon sink than Exp_OCO2. Comparing
310 Exp_OCO3 with Exp_OCO3&2, Exp_OCO3&2 shows stronger carbon sinks in temperate N. America,
311 southern Africa, Australia, and Europe; and weaker sinks in tropical S. America, northern Africa, and

312 boreal Asia; and elsewhere Exp_OCO3&2 shows sinks intermediate to the other two experiments.



313
 314 **Figure 3.** Spatial distribution of annual mean posterior terrestrial and oceanic carbon fluxes from 2020 to 2022,
 315 the difference between posterior and prior fluxes, and the distribution of terrestrial NEEs at different latitudes.
 316 (a, b, c, Exp_OCO3; d, e, f, Exp_OCO2; g, h, i, Exp_OCO3&2)

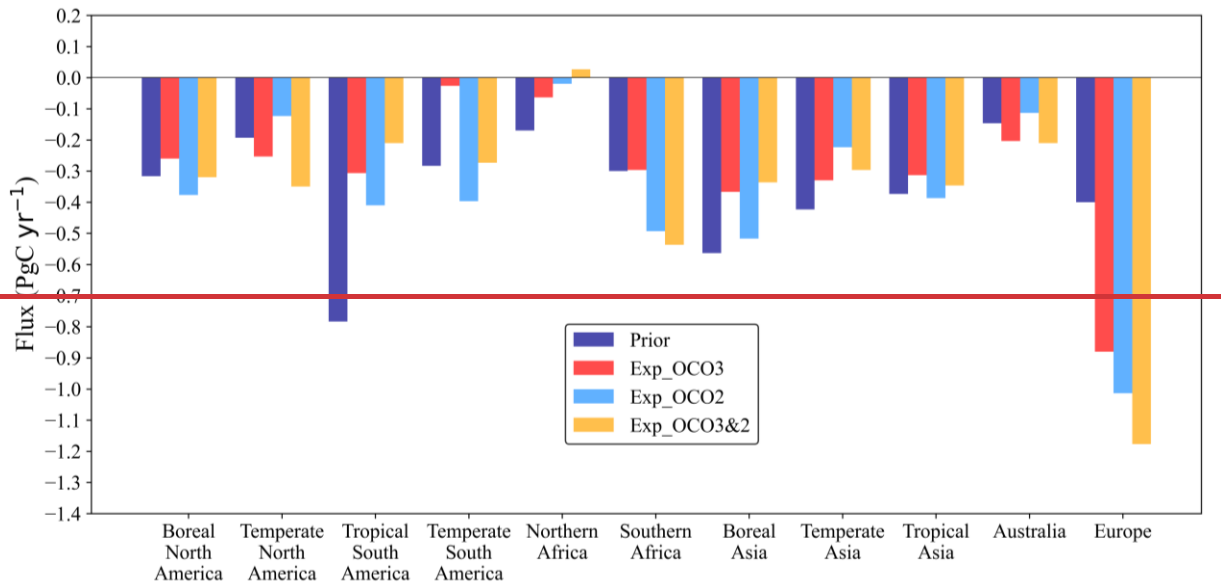
317
 318 The regions with more pronounced differences among experiments are temperate S. America and
 319 Europe. In Europe, the posterior fluxes of each inversion experiment show a pronounced carbon sink,
 320 which is significantly considerably larger than the prior flux, but the results of different experiments
 321 vary to some extent significantly, with NEEs ranging from -0.88 ± 0.24 to -1.18 ± 0.21 PgC yr⁻¹ (Table
 322 2), with Exp_OCO3&2 having the largest sink. In the temperate S. America, Exp_OCO3 exhibits a
 323 very weak carbon sink, whereas both Exp_OCO2 and Exp_OCO3&2 show a moderate carbon sink.
 324 One potential explanation for this discrepancy is that the XCO₂ concentration observed by OCO-3 in
 325 the temperate South America is higher than that observed by OCO-2 for the duration of the study
 326 period (by ~0.55 ppm). Consequently, in that assimilating the OCO-3 observations yields a weaker
 327 carbon sink. Compared with the prior flux, the posterior NEE in the tropical S. America shows a sig-
 328 nificant discrepancy, the prior flux show a very strong carbon sink of -0.78 ± 0.23 PgC yr⁻¹, whereas the

329 subsequent application of constraints from satellite observations resulted in a reduction of the carbon
 330 sinks by approximately 2 to 3 times, with values ranging from -0.21 ± 0.19 to -0.41 ± 0.20 PgC yr⁻¹.

331 Following the imposition of constraints derived from satellite observations, the carbon sinks on
 332 the Northern Hemisphere land are all enhanced, with the largest enhancement of 0.59 PgC yr⁻¹ in
 333 Exp_OCO3&2, followed by 0.19 and 0.36 PgC yr⁻¹ in Exp_OCO3 and Exp_OCO2, respectively.
 334 While in the tropics, the carbon sinks were all weakened, with Exp_OCO3 being weakened most, by
 335 0.67 PgC yr⁻¹, and the Exp_OCO2 and Exp_OCO3&2 being weakened by 0.37 and 0.59 PgC yr⁻¹,
 336 respectively; on Southern Hemisphere land, in Exp_OCO3, the sinks were weakened by 0.2 PgC yr⁻¹,
 337 whereas in Exp_OCO2 and Exp_OCO3&2, they were enhanced by 0.08 and 0.05 PgC yr⁻¹, respec-
 338 tively.

339 **Table 2.** Annual mean terrestrial fluxes (PgC yr⁻¹) in 2020-2022 for 11 TransCom-3 land regions, as well as for
 340 Northern Hemisphere land, Tropical land and Southern Hemisphere land. Includes the prior flux and the poste-
 341 rior fluxes from three inversion experiments.

Regions	Prior	Exp_OCO3	Exp_OCO2	Exp_OCO3&2
Boreal North America	-0.32 ± 0.16	-0.26 ± 0.14	-0.38 ± 0.13	-0.32 ± 0.13
Temperate North America	-0.19 ± 0.30	-0.25 ± 0.25	-0.12 ± 0.25	-0.35 ± 0.21
Tropical South America	-0.78 ± 0.23	-0.31 ± 0.21	-0.41 ± 0.20	-0.21 ± 0.19
Temperate South America	-0.28 ± 0.22	-0.03 ± 0.17	-0.40 ± 0.16	-0.27 ± 0.14
Northern Africa	-0.17 ± 0.28	-0.06 ± 0.24	-0.02 ± 0.23	0.03 ± 0.20
Southern Africa	-0.30 ± 0.24	-0.30 ± 0.19	-0.49 ± 0.17	-0.54 ± 0.16
Boreal Asia	-0.56 ± 0.26	-0.37 ± 0.24	-0.52 ± 0.21	-0.34 ± 0.23
Temperate Asia	-0.42 ± 0.23	-0.33 ± 0.20	-0.22 ± 0.19	-0.30 ± 0.18
Tropical Asia	-0.37 ± 0.13	-0.31 ± 0.12	-0.39 ± 0.11	-0.35 ± 0.11
Australia	-0.15 ± 0.09	-0.20 ± 0.08	-0.11 ± 0.08	-0.21 ± 0.07
Europe	-0.40 ± 0.26	-0.88 ± 0.24	-1.01 ± 0.19	-1.18 ± 0.21
Northern Hemisphere lands	-1.89 ± 0.56	-2.08 ± 0.49	-2.25 ± 0.44	-2.48 ± 0.44
Tropical lands	-1.65 ± 0.45	-0.98 ± 0.38	-1.28 ± 0.37	-1.06 ± 0.34
Southern Hemisphere lands	-0.43 ± 0.24	-0.23 ± 0.18	-0.51 ± 0.17	-0.48 ± 0.15



342
343 **Figure 4.** Annual average terrestrial carbon fluxes for the 11 TransCom-3 land regions in 2020-2022.

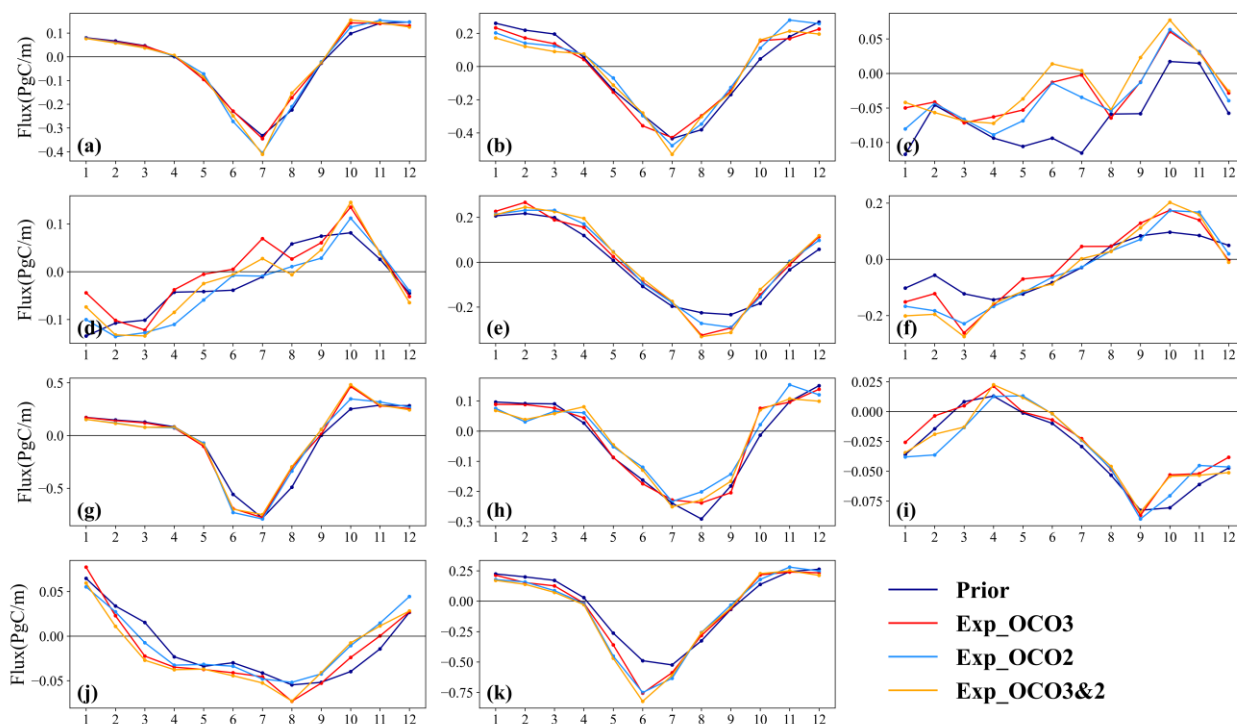
344 4.3 Seasonal cycle of NEE

345 Figure 45 illustrates the seasonal cycle of NEE for each TransCom-3 region. The posterior NEEs
 346 of different experiments are in good agreement on the seasonal cycle in most regions. In the Northern
 347 Hemisphere, the seasonal cycles of NEE in boreal N. America, temperate N. America, boreal Asia,
 348 temperate Asia, and Europe show relatively consistent trends. Carbon sinks in these regions generally
 349 occur from May to September and carbon sources from October to April. Significant Large differences
 350 are evident in the strength of the carbon sinks observed in different regions, with different months in
 351 which the strongest carbon sinks occur. Boreal N. America, temperate N. America, and boreal Asia
 352 have the strongest carbon sinks in July, temperate Asia has the peak in July or August, and Europe has
 353 the strongest sinks in June. In the Southern Hemisphere, the southern Africa and temperate S. America
 354 have more consistent seasonal cycles, with their carbon sources occurring roughly from July to De-
 355 cember and sinks from January to June. The strongest carbon sources all occur in October, and the
 356 strongest sinks occur around March. In Australia, carbon sinks occur mainly from March to October,
 357 with the peak occurring in August. In the tropics, southern Africa shows a seasonal cycle opposite to
 358 that of northern Africa, and carbon sinks occur from January to July with the strongest carbon sinks
 359 occurring near March. Tropical Asia shows a carbon sink in most months, with the strongest sink in
 360 September. The seasonal cycle in tropical S. America is more complex, with the strongest carbon

361 source in October. In general, seasonal amplitudes are small in the tropics and large in the northern
362 regions. The averaged seasonal amplitudes of the three inversion experiments in the boreal Asia, Eu-
363 rope, and temperate N. America are 1.17, 0.97, and 0.72 PgC yr⁻¹, respectively, while the seasonal
364 amplitudes in tropical Asia and S. America are about 0.10 PgC yr⁻¹.

365 The regions where the difference between the prior and posterior NEEs is particularly pronounced
366 are tropical S. America, southern Africa, Australia, and Europe. In the tropical S. America, the prior
367 NEE is a significant sink from May to July, but after constraints from satellite observations, the carbon
368 sink decreases significantly, even approaching neutral in June and July, and furthermore, in September
369 and October, the sink also decreases significantly compared to the a priori. In southern Africa, the
370 carbon sink is significantly stronger from January to March compared to the a priori, and conversely,
371 the carbon source is significantly stronger in October and November. In Australia, the carbon sink is
372 significantly increased from January to August and decreased in October and November compared to
373 the a priori. In Europe, there is a significant increase in the carbon sinks from May to June compared
374 to the a priori.

375 As described in Section 4.2 that in temperate N. America, northern Africa, temperate Asia, and
376 Australia, Exp_OCO3 shows a stronger sink than Exp_OCO2, which mainly occurs in May and June
377 in temperate N. America, in August and September in northern Africa, from April to September in
378 temperate Asia, and in Australia except for July. In other regions, Exp_OCO3 has weaker sinks than
379 Exp_OCO2. In the high latitudinal regions, on the one hand, the carbon sinks in June and July of the
380 Exp_OCO3 are generally smaller than those of Exp_OCO2, and on the other hand, the carbon source
381 in October is significantly higher than that of Exp_OCO2, while in the tropics, the carbon sink is lower
382 than that of Exp_OCO2 almost all year round. Compared to Exp_OCO3, Exp_OCO3&2 shows
383 stronger carbon sinks in temperate N. America, southern Africa, Australia, and Europe, mainly in sum-
384 mer; and weaker sinks in tropical S. America, northern Africa, and boreal Asia, mainly in autumn.
385 Elsewhere Exp_OCO3&2 shows carbon sinks intermediate to the other two experiments.



386 **Figure 45.** Averaged prior and posterior seasonal cycle of NEE in different TransCom-3 regions during 2020–
 387 2022; (a) boreal N. America, (b) temperate N. America, (c) tropical S. America, (d) temperate S. America, (e)
 388 northern Africa, (f) southern Africa, (g) boreal Asia, (h) temperate Asia, (i) tropical Asia, (j) Australia, (k) Eu-
 389 rope.

390 4.4 Evaluation against independent observations

391 As shown in Figure 56, observations from 66 surface flask sites were used to evaluate the poste-
 392 rior fluxes. The prior and posterior CO₂ concentrations were simulated by the MOZART-4 model using
 393 the corresponding prior and posterior fluxes, as described in Section 3. The overall assessment results
 394 of the individual inversion experiments on a global scale are shown in Table 3. The results show that
 395 the mean BIAS, MAE, and RMSE between the prior CO₂ concentrations and surface flask observations
 396 are -1.82, 3.27, and 5.01 ppm, respectively. The prior BIAS shows a pronounced negative bias, which
 397 can be attributed to the fact that the prior NEE in 2019 (generated by the spin-up stage) was, on average,
 398 approximately 3.5 PgC less than the posterior NEE. This part of the NEE will has an impact on the
 399 subsequent inversion. After constraints using the XCO₂ retrievals, the biases of the three experiments
 400 are reduced significantly compared to the a priori, indicating that the surface carbon fluxes have been

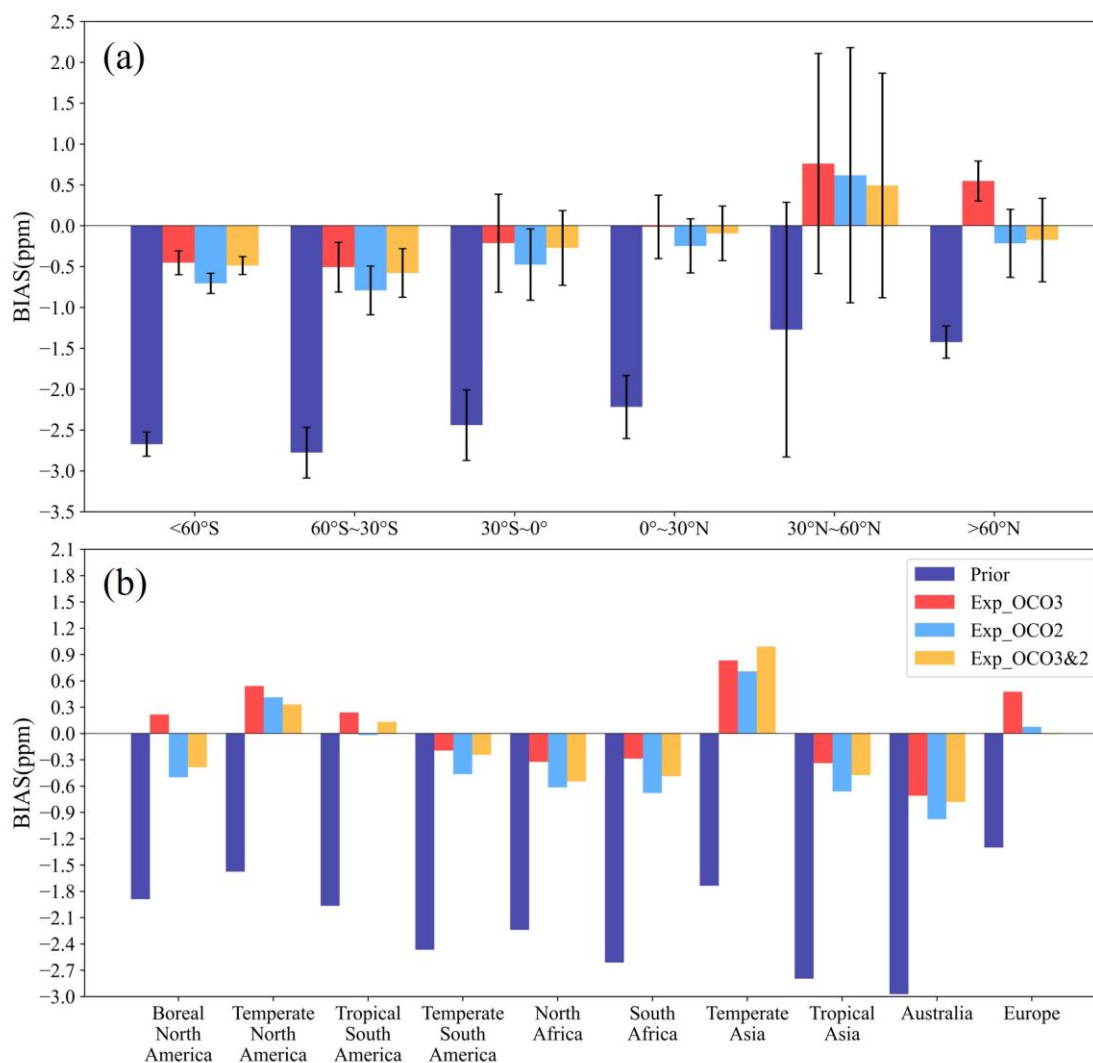
401 improved. A comparison of the three inversion experiments reveals that Exp_OCO3 exhibits the largest
 402 BIAS, while Exp_OCO3&2 exhibits the lowest MAE and RMSE.

403 **Table 3.** Error statistics between the simulated CO₂ concentrations and surface flask observations (ppm).

	BIAS	MAE	RMSE
Prior	-1.82	3.27	5.01
Exp_OCO3	0.32	2.44	4.56
Exp_OCO2	0.02	2.42	4.49
Exp_OCO3&2	0.05	2.34	4.47

410 Figure 6a-5a and 6b-5b illustrate the BIAS of the individual inversion experiments at different
 411 latitudinal zones and in different TransCom-3 land regions. In all latitudinal bands and all land regions,
 412 the CO₂ concentrations modelled by the a priori fluxes have the largest negative BIAS, which is greater
 413 than -1.2 ppm in all cases. Across latitudinal zones, in the Southern Hemisphere, and south of 30°N
 414 latitude, the Exp_OCO3 had the smallest BIAS, which is ~~significantly~~ smaller than the Exp_OCO2
 415 and comparable to the results of the Exp_OCO3&2. However, in the mid to high latitudes of the North-
 416 ern Hemisphere, the BIAS of the Exp_OCO3 is ~~significantly~~ higher than those of the Exp_OCO2 and
 417 Exp_OCO3&2. Especially in the region north of 60°N latitude, the Exp_OCO3 exhibits a significant
 418 positive BIAS, while the Exp_OCO2 and Exp_OCO3&2 both exhibit small negative BIAS. This sug-
 419 gests that the carbon sinks at mid to high latitudes were underestimated ~~due to the lack of observational~~
 420 ~~data for the OCO-3 north of 52°N latitude.~~ We also find that the OCO-3 retrievals help with the lack
 421 of space-based XCO₂ observations in the tropics compared to OCO-2. The BIAS of Exp_OCO3&2 is
 422 smaller than Exp_OCO2 in the region from 30°S to 30°N. Meanwhile, the BIAS of Exp_OCO3&2 is
 423 also smaller than Exp_OCO2 in southern Africa, northern Africa and tropical Asia. Furthermore, we
 424 can find that the BIAS can be further reduced in the mid to high latitudes of the Northern Hemisphere
 425 after the addition of assimilated OCO-3 observations compared to the Exp_OCO2. In different Trans-
 426 Com-3 land regions, the BIAS of the three inversion experiments is less than ±0.6 ppm, except in the
 427 temperate Asia. In Africa, temperate S. America, tropical Asia, and Australia, the Exp_OCO3 had the
 428 smallest BIAS, while the BIAS of Exp_OCO3&2 was between those of Exp_OCO3 and Exp_OCO2.

429 However, in temperate N. America and Europe, the Exp_ OCO3 has the largest BIAS, followed by the
 430 Exp_ OCO2, while the Exp_ OCO3&2 has the smallest BIAS. ~~This suggests that since OCO-3 obser-~~
 431 ~~vations are only available between 52 degrees north and south latitudes, assimilating only OCO-3~~
 432 ~~observations will result in a significant BIAS in the middle and high latitudes. Conversely, joint as-~~
 433 ~~similation of OCO-2 and OCO-3 observations can compensate for the limitations of the OCO-3 obser-~~
 434 ~~vations, thereby achieving the most optimal assimilation outcomes.~~



435
 436 **Figure 56.** The prior and posterior CO₂ BIAS(a) at different latitudinal zones and (b) in different land
 437 regions.

438 **4.5 Discussion**

439 In most of the previous studies that used OCO-2 XCO₂ to invert surface carbon fluxes, the OG
 440 data were not used (e.g., Peiro et al., 2022; Byrne et al., 2023), the reason is that the OG XCO₂ may

441 have larger uncertainties, inversions assimilating OCO-2 OG retrievals produced unrealistic results of
442 annual global ocean sinks (Peiro et al., 2022). In addition to its large uncertainties, we believe that
443 another reason for the poor assimilation performance of OG is the relatively homogeneous distribution
444 of XCO₂ on ocean, causing a large correlation of the model-data biases among different XCO₂ obser-
445 vations within a same region, which leads to observations at the same region having the same direction
446 of adjustment for surface fluxes, and thus leads to a significant overestimated or underestimated of
447 ocean carbon sink. Because of this, some assimilation algorithms (e.g., EnSRF) can only achieve better
448 assimilation results when the model-data biases between observations have relatively small correlation
449 or are uncorrelated. Therefore, in this study, we set the OG data with larger uncertainties than the
450 LNLG data, and re-grided it at a coarser spatial resolution of 5° × 5° . The results show that under
451 this scheme, the inverted ocean sink is reasonable, with value of -2.6 PgC yr⁻¹ (Table 1). In addition,
452 in order to compare the scheme that we have adopted in this study with the previous scheme that do
453 not assimilate the OG, we added three additional inversion experiments, in which only the LNLG data
454 were assimilated (Table S1). It could be found that all the three inversion experiments without OG
455 observations place smaller constraints on the ocean fluxes compared to the original experiments, with
456 the posterior ocean fluxes remaining almost identical to the prior ocean fluxes. Correspondingly, the
457 inverted global land sink as well as the sinks in most regions show a slight decrease (Tables S2 and
458 S3). Evaluations in comparison with *in-situ* observations showed that there are some increases in the
459 a posteriori concentration biases for all three experiments after removing OG. For example, for the
460 experiments assimilating OCO-2 data, the mean bias increased from 0.02 to 0.14 ppm (Table S4). This
461 suggests that assimilating OG data with our method can improve the inversions somewhat compared
462 to removing OG.

463 Since OCO-3 has similar observation uncertainties of XCO₂ with OCO-2 (Taylor et al., 2023), the
464 poor performance of assimilating OCO-3 XCO₂ retrievals (Exp_OCO3) may be related to that 1)
465 OCO-3 lacks observations beyond 52° North and South latitudes (Figure 1a); 2) the observation time
466 different from OCO-2; and 3) its spatial coverage between 52°S and 52°N. We first examined weekly
467 changes in the data amount of OCO-3 using the re-grided data as described in Section 2.3, and found

468 that there are very significant cyclical fluctuations in the data amount from OCO-3 (Figure S4a). Every
469 8 weeks or so, there is a trough in the data amount. There is a difference of about 5 times between the
470 weeks with the highest and the lowest data amount, and in the weeks with least data amount, there
471 were essentially no observations in the northern hemisphere (Figure S4b). This implies that the surface
472 carbon fluxes are largely unconstrained in the Northern Hemisphere, especially at mid- to high-lati-
473 tudes, during the weeks with low observational data, resulting in poorer assimilation performance than
474 for OCO-2. For the observation time, all observations of OCO-2 were at 1:30 p.m. local time (LST),
475 whereas that of OCO-3 were variable, with only about 14% of the observations near 13:30 p.m. LST
476 and about 54% in the morning or after 4:00 p.m. LST (Figure S1). For reasons such as coarser model
477 resolution, the global atmospheric chemical transport models generally simulate atmospheric concen-
478 trations better only in the afternoon, when boundary layer heights are at their highest and atmospheric
479 mixing is at its best, so assimilating these observations in the morning and after 4 p.m. LST may result
480 in poorer inversions due to the greater simulation bias of the atmospheric transport models at these
481 times of day.

482 In order to quantify these effects, we added another 3 additional inversion experiments, which
483 were named as Exp_OCO2r, Exp_OCO3tc, and Exp_OCO2ts (Table S1). In Exp_OCO2r, only the
484 OCO-2 XCO₂ retrievals located between 52°S and 52°N retrievals were assimilated, in Exp_OCO3tc,
485 all the observation times of the OCO-3 XCO₂ retrievals were changed to 1.30 p.m. LST, and in
486 Exp_OCO3ts, only OCO-3 data with observation times between 12 and 3 p.m. LST were assimilated.
487 When the OCO-2 data beyond 52° North and South latitudes were also removed (Exp_OCO2r), the
488 NEE estimates, both globally and for individual regions, are close to those of the Exp_OCO3 experi-
489 ment, especially in the high latitude region of Europe and boreal North America, the inverted NEEs
490 are almost identical to those of the Exp_OCO3 experiment (Table S2 and S3), and the bias of a poste-
491 riori concentrations from observations at high latitudes is close to that of the OCO-3 experiment (Fig-
492 ure S3). However, globally, compared to the OCO-3 experiment, the Exp_OCO2r experiment still has
493 smaller the deviation between the global net flux and the observed annual growth rate (Table S2), and
494 smaller the global mean bias of the posterior concentrations (Table S4). This suggests that the lack of

495 observations of OCO-3 beyond 52° North and South latitudes does have a significant impact on the
496 inversion results. In addition, it can also be noted that at mid-latitudes, the bias of Exp_OCO2r is also
497 smaller than the OCO-3 experiment, which may be caused by the significant fluctuations in the data
498 amount of OCO-3 (Figure S4). When we changed all the observation times of the OCO-3 XCO₂ re-
499 trievals to 1.30 p.m. LST (Exp_OCO3tc), although we are not actually able to do so, the inversion does
500 show a significant improvement compared to Exp_OCO3. However, if we only select the data with
501 observation time between 12:00 and 3:00 p.m. LST (Exp_OCO3ts), the deviation between the global
502 net flux and the observed annual growth rate, and the mean biases of the posterior concentrations at
503 most latitudes are larger than those of Exp_OCO3 (Table S2 and Figure S3), indicating a poorer per-
504 formance than Exp_OCO3. The probably reason is that the data number of observations is substantially
505 reduced at this time (Figure S2), which leads to a substantial weakening of the observational constraints
506 on surface carbon fluxes (Figure S5).

507

508 **5 Summary and Conclusion**

509 In this study, we constrained terrestrial NEEs for the period from 1 August 2019 to 31 December
510 2022 using the OCO-2 and OCO-3 XCO₂ retrievals and the GCASv2 system, and analyzed the inver-
511 sion results from 2020 to 2022. We conducted three inversion experiments for separately and jointly
512 assimilating the OCO-2 and OCO-3 XCO₂ retrievals, to explore the impact of the OCO-3 XCO₂ re-
513 trievals on the constraints of global terrestrial NEEs. The prior and posterior CO₂ mixing ratios ob-
514 tained from forward simulations using the prior and posterior fluxes are analysed in comparison with
515 observations from 66 surface flask sites.

516 Globally, the terrestrial carbon sink from the Exp_OCO3 is smaller than the prior, while the ter-
517 restrial carbon sinks from the other two inversion experiments are slightly larger than the prior, but the
518 difference is small. The global net carbon flux from the Exp_OCO3&2 is very close to the observed
519 atmospheric CO₂ growth rate. Regionally, the posterior NEEs for most terrestrial regions show a car-
520 bon sink, with Europe showing a very strong sink and North Africa close to carbon neutrality. In the
521 Northern Hemisphere, the carbon sinks are enhanced, with the Exp_OCO3&2 being the most enhanced
522 by 0.59 PgC yr⁻¹ and the Exp_OCO3 and Exp_OCO2 by 0.19 and 0.36 PgC yr⁻¹, respectively. In the

523 tropics, the carbon sinks are weakened, with the Exp_OCO3 being the most weakened by 0.67 PgC
524 yr⁻¹, and the Exp_OCO2 and Exp_OCO3&2 sinks being weakened by 0.37 and 0.59 PgC yr⁻¹, respec-
525 tively; in the southern land, the sink inverted in Exp_OCO3 is weakened by 0.2 PgC yr⁻¹, whereas
526 those in the Exp_OCO2 and Exp_OCO3&2 are enhanced, by 0.08 and 0.05 PgC yr⁻¹, respectively.

527 On a global scale, the BIAS between the prior CO₂ concentrations and surface flask observations
528 is -1.82 ppm, with a MAE of 3.27 ppm and a RMSE of 5.01 ppm. The deviations between the posterior
529 CO₂ concentrations and surface flask observations for all three inversions are reduced to different de-
530 grees from the prior, especially for the BIAS, which decreased to 0.32, 0.02, and 0.05 ppm by
531 Exp_OCO3, Exp_OCO2, and Exp_OCO3&2, respectively. ~~This suggests that since OCO-3 only has
532 observations from 52°S to 52°N, assimilating OCO-3 observations alone may lead to an underestima-
533 tion of the terrestrial carbon sink, and the joint assimilation of OCO-2 and OCO-3 XCO₂ retrievals is
534 required for better estimation of the global terrestrial carbon sources and sinks. The reasons for the
535 poor performance of assimilating OCO-3 XCO₂ alone are, on the one hand, the fact that it is only
536 available between 52° S and 52°N, which leads to a lack of observational constraints on the carbon
537 sinks at high latitudes, and the large fluctuations in the amount of observational data, which leads to
538 significant differences in observational constraints at mid-latitudes at different times; on the other hand,
539 its varied observation time also affect the inversions, but even choosing afternoon observations does
540 not improve the inversions because the amount of observed data drops significantly. Therefore, a better
541 option for the future would be to jointly assimilate the OCO-2 XCO₂ data and the OCO-3 XCO₂ re-
542 trievals observed in the afternoon (12:00 to 16:00 LST).~~

543
544 **Code availability.** The code of the GCASv2 system is available to the community and can be accessed
545 upon request from Fei Jiang(jiangf@nju.edu.cn) at Nanjing University.

546 **Data availability.** The OCO-2 and OCO-3 data used in this study is available at [https://www](https://www.earthdata.nasa.gov)
547 [w.earthdata.nasa.gov](https://www.earthdata.nasa.gov). The FOSSIL carbon emissions of GCP-GridFEDv2023.1 is available at
548 <https://doi.org/10.5281/zenodo.8386803>. The FIRE carbon emissions GFED 4.1s is available at
549 https://daac.ornl.gov/VEGETATION/guides/fire_emissions_v4_R1.html. The results of three in
550 version experiments and evaluation are publicly available at [https://doi.org/10.5281/zenodo.112](https://doi.org/10.5281/zenodo.11239535)
551 [39535](https://doi.org/10.5281/zenodo.11239535).

552
553 **Author contributions.** XW and FJ designed the research. XW ran the model, analyzed the results
554 and wrote the paper. HW and ZZ collected the OCO-2 and OCO-3 XCO₂ retrievals. MW, JW, WH,
555 WJ and JC participated in the discussion of the inversion results and provided revisions before the
556 paper was submitted.

557

558 **Competing interests.** The author has declared that none of the authors has any competing interests.

559

560 **Financial support.** This work is supported by the National Key R&D Program of China (Grant No:
561 2023YFB3907404), ~~and~~ the National Natural Science Foundation of China (Grant No. 42377102),
562 [and the Fengyun Application Pioneering Project \(Grant No: FY-APP-2022.0505\)](#).

563

564 **Acknowledgments.** The OCO-2 and OCO-3 data are produced by the OCO project at the Jet Propul-
565 sion Laboratory, California Institute of Technology, and obtained from the data archive at the NASA
566 Goddard Earth Science Data and Information Services Center. We acknowledge all atmospheric data
567 providers to obspack_co2_1_GLOBALVIEWplus_v9.1_2023-12-08. We are also grateful to the
568 High-Performance Computing Center (HPCC) of Nanjing University for doing the numerical calcu-
569 lations in this paper on its blade cluster system.

570

571 **References**

572 Basu, S., Guerlet, S., Butz, A., Houweling, S., Hasekamp, O., Aben, I., Krummel, P., Steele, P., Langen-
573 felds, R., Torn, M., Biraud, S., Stephens, B., Andrews, A., and Worthy, D.: Global CO₂ fluxes
574 estimated from GOSAT retrievals of total column CO₂, Atmos. Chem. Phys., 13, 8695–8717,

- 575 <https://doi.org/10.5194/acp-13-8695-2013>, 2013.
- 576 Botta, A., Ramankutty, N., and Foley, J. A.: LBA-ECO LC-04 IBIS Model Simulations for the Amazon
577 and Tocantins Basins: 1921-1998, <https://doi.org/10.3334/ORNLDAAAC/1139>, 2012.
- 578 Bousquet, P., Peylin, P., Ciais, P., Le Quéré, C., Friedlingstein, P., and Tans, P. P.: Regional Changes in
579 Carbon Dioxide Fluxes of Land and Oceans Since 1980, *Science*, 290, 1342-1346,
580 <https://doi.org/10.1126/science.290.5495.1342>, 2000.
- 581 Byrne, B., Liu, J., Lee, M., Baker, I., Bowman, K. W., Deutscher, N. M., Feist, D. G., Griffith, D. W.
582 T., Iraci, L. T., Kiel, M., Kimball, J. S., Miller, C. E., Morino, I., Parazoo, N. C., Petri, C., Roehl,
583 C. M., Sha, M. K., Strong, K., Velazco, V. A., Wennberg, P. O., and Wunch, D.: Improved con-
584 straints on northern extratropical CO₂ fluxes obtained by combining surface-based and space-
585 based atmospheric CO₂ measurements, *J. Geophys. Res.: Atmos.*, 125, e2019JD032029,
586 <https://doi.org/10.1029/2019JD032029>, 2020.
- 587 Byrne, B., Liu, J., Lee, M., Yin, Y., Bowman, K. W., Miyazaki, K., Norton, A. J., Joiner, J., Pollard, D.
588 F., Griffith, D. W. T., Velazco, V. A., Deutscher, N. M., Jones, N. B., and Paton - Walsh, C.: The
589 carbon cycle of southeast Australia during 2019–2020: Drought, fires, and subsequent recovery,
590 *AGU Advances*, 2, e2021AV000469, <https://doi.org/10.1029/2021AV000469>, 2021.
- 591 Byrne, B., Liu, J., Yi, Y., Chatterjee, A., Basu, S., Cheng, R., Doughty, R., Chevallier, F., Bowman, K.
592 W., Parazoo, N. C., Crisp, D., Li, X., Xiao, J., Sitch, S., Guenet, B., Deng, F., Johnson, M. S.,
593 Philip, S., McGuire, P. C., and Miller, C. E.: Multi-year observations reveal a larger than expected
594 autumn respiration signal across northeast Eurasia, *Biogeosciences*, 19, 4779–4799,
595 <https://doi.org/10.5194/bg-19-4779-2022>, 2022.
- 596 Byrne, B., Baker, D. F., Basu, S., Bertolacci, M., Bowman, K. W., Carroll, D., Chatterjee, A., Cheval-
597 lier, F., Ciais, P., Cressie, N., Crisp, D., Crowell, S., Deng, F., Deng, Z., Deutscher, N. M., Dubey,
598 M. K., Feng, S., García, O. E., Griffith, D. W. T., Herkommer, B., Hu, L., Jacobson, A. R., Janar-
599 danan, R., Jeong, S., Johnson, M. S., Jones, D. B. A., Kivi, R., Liu, J., Liu, Z., Maksyutov, S.,
600 Miller, J. B., Miller, S. M., Morino, I., Notholt, J., Oda, T., O'Dell, C. W., Oh, Y.-S., Ohyama, H.,
601 Patra, P. K., Peiro, H., Petri, C., Philip, S., Pollard, D. F., Poulter, B., Remaud, M., Schuh, A., Sha,
602 M. K., Shiomi, K., Strong, K., Sweeney, C., Té, Y., Tian, H., Velazco, V. A., Vrekoussis, M.,
603 Warneke, T., Worden, J. R., Wunch, D., Yao, Y., Yun, J., Zammit-Mangion, A., and Zeng, N.:
604 National CO₂ budgets (2015–2020) inferred from atmospheric CO₂ observations in support of the
605 global stocktake, *Earth Syst. Sci. Data*, 15, 963–1004, <https://doi.org/10.5194/essd-15-963-2023>,
606 2023.
- 607 Chen, H., He, W., Liu, J., Nguyen, N. T., Chevallier, F., Yang, H., Lv, Y., Huang, C., Rödenbeck, C.,
608 Miller, S., Jiang, F., Liu, J., Johnson, M., Philip, S., Liu, Z., Zeng, N., Basu, S., and Baker, D.:
609 Satellite-detected large CO₂ release in southwestern North America during the 2020–2021
610 drought and associated wildfires, *Environ. Res. Lett.*, 19, <https://doi.org/10.1088/1748-9326/ad3cf7>, 2024.
- 612 Chen, J. M., Ju, W., Ciais, P., Viovy, N., Liu, R., Liu, Y., and Lu, X.: Vegetation structural change since

613 1981 significantly enhanced the terrestrial carbon sink, *Nat. Commun.*, 10,
614 <https://doi.org/10.1038/s41467-019-12257-8>, 2019.

615 Crisp, D., Pollock, H. R., Rosenberg, R., Chapsky, L., Lee, R. A. M., Oyafuso, F. A., Frankenberg, C.,
616 O'Dell, C. W., Bruegge, C. J., Doran, G. B., Eldering, A., Fisher, B. M., Fu, D., Gunson, M. R.,
617 Mandrake, L., Osterman, G. B., Schwandner, F. M., Sun, K., Ta-ylor, T. E., Wennberg, P. O., and
618 Wunch, D.: The on-orbit performance of the Orbiting Carbon Observatory-2 (OCO-2) instrument
619 and its radiometrically calibrated products, *Atmos. Meas. Tech.*, 10, 59–81,
620 <https://doi.org/10.5194/amt-10-59-2017>, 2017.

621 Crowell, S., Baker, D., Schuh, A., Basu, S., Jacobson, A. R., Chevallier, F., Liu, J., Deng, F., Feng, L.,
622 McKain, K., Chatterjee, A., Miller, J. B., Stephens, B. B., Eldering, A., Crisp, D., Schimel, D.,
623 Nassar, R., O'Dell, C. W., Oda, T., Sweeney, C., Palmer, P. I., and Jones, D. B. A.: The 2015–2016
624 carbon cycle as seen from OCO-2 and the global in situ network, *Atmos. Chem. Phys.*, 19, 9797–
625 9831, <https://doi.org/10.5194/acp-19-9797-2019>, 2019.

626 Eldering, A., Boland, S., Solish, B., Crisp, D., Kahn, P., and Gunson, M.: High precision atmospheric
627 CO₂ measurements from space: The design and implementation of OCO-2, 2012 IEEE Aerospace
628 Conference, 3-10 March 2012, 1-10, <https://doi.org/10.1109/AERO.2012.6187176>, 2012.

629 Eldering, A., O'Dell, C. W., Wennberg, P. O., Crisp, D., Gunson, M. R., Viatte, C., Avis, C., Braverman,
630 A., Castano, R., Chang, A., Chapsky, L., Cheng, C., Connor, B., Dang, L., Doran, G., Fisher, B.,
631 Frankenberg, C., Fu, D., Granat, R., Hobbs, J., Lee, R. A. M., Mandrake, L., McDuffie, J., Miller,
632 C. E., Myers, V., Natraj, V., O'Brien, D., Osterman, G. B., Oyafuso, F., Payne, V. H., Pollock, H.
633 R., Polonsky, I., Roehl, C. M., Rosenberg, R., Schwandner, F., Smyth, M., Tang, V., Taylor, T. E.,
634 To, C., Wunch, D., and Yoshimizu, J.: The Orbiting Carbon Observatory-2: first 18 months of
635 science data products, *Atmos. Meas. Tech.*, 10, 549–563, [https://doi.org/10.5194/amt-10-549-](https://doi.org/10.5194/amt-10-549-2017)
636 2017, 2017.

637 Emmons, L. K., Walters, S., Hess, P. G., Lamarque, J.-F., Pfister, G. G., Fillmore, D., Granier, C.,
638 Guenther, A., Kinnison, D., Laepple, T., Orlando, J., Tie, X., Tyndall, G., Wiedinmyer, C., Baugh-
639 cum, S. L., and Kloster, S.: Description and evaluation of the Model for Ozone and Related chem-
640 ical Tracers, version 4 (MOZART-4), *Geosci. Model Dev.*, 3, 43–67, [https://doi.org/10.5194/gmd-](https://doi.org/10.5194/gmd-3-43-2010)
641 3-43-2010, 2010.

642 Enting, I.G., Newsam, G.N. Atmospheric constituent inversion problems: Implications for baseline
643 monitoring. *J Atmos Chem* 11, 69–87, <https://doi.org/10.1007/BF00053668>, 1990.

644 Feng, S., Jiang, F., Wu, Z., Wang, H., Ju, W., and Wang, H.: CO Emissions Inferred From Surface CO
645 Observations Over China in December 2013 and 2017, *J. Geophys. Res.: Atmos.*, 125,
646 <https://doi.org/10.1029/2019jd031808>, 2020.

647 Friedlingstein, P., O'Sullivan, M., Jones, M. W., Andrew, R. M., Bakker, D. C. E., Hauck, J., Land-
648 schützer, P., Le Quéré, C., Luijkx, I. T., Peters, G. P., Peters, W., Pongratz, J., Schwingshackl, C.,
649 Sitch, S., Canadell, J. G., Ciais, P., Jackson, R. B., Alin, S. R., Anthoni, P., Barbero, L., Bates, N.
650 R., Becker, M., Bellouin, N., Decharme, B., Bopp, L., Brasika, I. B. M., Cadule, P., Chamberlain,

- 651 M. A., Chandra, N., Chau, T.-T.-T., Chevallier, F., Chini, L. P., Cronin, M., Dou, X., Enyo, K.,
652 Evans, W., Falk, S., Feely, R. A., Feng, L., Ford, D. J., Gasser, T., Ghattas, J., Gkritzalis, T., Grassi,
653 G., Gregor, L., Gruber, N., Gürses, Ö., Harris, I., Hefner, M., Heinke, J., Houghton, R. A., Hurtt,
654 G. C., Iida, Y., Ilyina, T., Jacobson, A. R., Jain, A., Jarníková, T., Jersild, A., Jiang, F., Jin, Z., Joos,
655 F., Kato, E., Keeling, R. F., Kennedy, D., Klein Goldewijk, K., Knauer, J., Korsbakken, J. I.,
656 Körtzinger, A., Lan, X., Lefèvre, N., Li, H., Liu, J., Liu, Z., Ma, L., Marland, G., Mayot, N.,
657 McGuire, P. C., McKinley, G. A., Meyer, G., Morgan, E. J., Munro, D. R., Nakaoka, S.-I., Niwa,
658 Y., O'Brien, K. M., Olsen, A., Omar, A. M., Ono, T., Paulsen, M., Pierrot, D., Pocock, K., Poulter,
659 B., Powis, C. M., Rehder, G., Resplandy, L., Robertson, E., Rödenbeck, C., Rosan, T. M.,
660 Schwinger, J., Séférian, R., Smallman, T. L., Smith, S. M., Sospedra-Alfonso, R., Sun, Q., Sutton,
661 A. J., Sweeney, C., Takao, S., Tans, P. P., Tian, H., Tilbrook, B., Tsujino, H., Tubiello, F., van der
662 Werf, G. R., van Ooijen, E., Wanninkhof, R., Watanabe, M., Wimart-Rousseau, C., Yang, D., Yang,
663 X., Yuan, W., Yue, X., Zaehle, S., Zeng, J., and Zheng, B.: Global Carbon Budget 2023, *Earth*
664 *Syst. Sci. Data*, 15, 5301–5369, <https://doi.org/10.5194/essd-15-5301-2023>, 2023.
- 665 Gurney, K. R., Law, R. M., Denning, A. S., Rayner, P. J., Baker, D., Bousquet, P., Bruhwiler, L., Chen,
666 Y.-H., Ciais, P., Fan, S., Fung, I. Y., Gloor, M., Heimann, M., Higuchi, K., John, J., Maki, T.,
667 Maksyutov, S., Masarie, K., Peylin, P., Prather, M., Pak, B. C., Randerson, J., Sarmiento, J.,
668 Taguchi, S., Takahashi, T., and Yuen, C.-W.: Towards robust regional estimates of CO₂ sources
669 and sinks using atmospheric transport models, *Nature*, 415, 626-630,
670 <https://doi.org/10.1038/415626a>, 2002.
- 671 Hall, B. D., Crotwell, A. M., Kitzis, D. R., Mefford, T., Miller, B. R., Schibig, M. F., and Tans, P. P.:
672 Revision of the World Meteorological Organization Global Atmosphere Watch (WMO/GAW)
673 CO₂ calibration scale, *Atmos. Meas. Tech.*, 14, 3015–3032, [https://doi.org/10.5194/amt-14-3015-](https://doi.org/10.5194/amt-14-3015-2021)
674 [2021](https://doi.org/10.5194/amt-14-3015-2021), 2021.
- 675 Hansen, J., Sato, M., Russell, G., and Kharecha, P.: Climate sensitivity, sea level and atmospheric
676 carbon dioxide, *Philos. Trans. R. Soc., A*, 371, <https://doi.org/10.1098/rsta.2012.0294>, 2013.
- 677 He, W., Jiang, F., Wu, M., Ju, W., Scholze, M., Chen, J. M., Byrne, B., Liu, J., Wang, H., Wang, J.,
678 Wang, S., Zhou, Y., Zhang, C., Nguyen, N. T., Shen, Y., and Chen, Z.: China's Terrestrial Carbon
679 Sink Over 2010–2015 Constrained by Satellite Observations of Atmospheric CO₂ and Land Sur-
680 face Variables, *J. Geophys. Res.: Biogeosci.*, 127, e2021JG006644,
681 <https://doi.org/10.1029/2021JG006644>, 2022.
- 682 He, W., Jiang, F., Ju, W., Chevallier, F., Baker, D. F., Wang, J., Wu, M., Johnson, M. S., Philip, S.,
683 Wang, H., Bertolacci, M., Liu, Z., Zeng, N., and Chen, J. M.: Improved Constraints on the Recent
684 Terrestrial Carbon Sink Over China by Assimilating OCO-2 XCO₂ Retrievals, *J. Geophys. Res.:*
685 *Atmos.*, 128, e2022JD037773, <https://doi.org/10.1029/2022JD037773>, 2023a.
- 686 He, W., Jiang, F., Ju, W., Byrne, B., Xiao, J., Nguyen, N. T., Wu, M., Wang, S., Wang, J., Rödenbeck,
687 C., Li, X., Scholze, M., Monteil, G., Wang, H., Zhou, Y., He, Q., and Chen, J. M.: Do State-Of-
688 The-Art Atmospheric CO₂ Inverse Models Capture Drought Impacts on the European Land Car-
689 bon Uptake?, *J. Adv. Model. Earth Syst.*, 15, e2022MS003150,

- 690 <https://doi.org/10.1029/2022MS003150>, 2023b.
- 691 [Houtekamer, P. L., and Mitchell, H. L.: A sequential ensemble Kalman filter for atmospheric data as
692 simulation, *Monthly Weather Review*, 129\(1\), 123-137, \[https://doi.org/10.1175/1520-
693 0493\\(2001\\)129<0123:ASEKFF>2.0.CO;2\]\(https://doi.org/10.1175/1520-0493\(2001\)129<0123:ASEKFF>2.0.CO;2\), 2001.](https://doi.org/10.1175/1520-0493(2001)129<0123:ASEKFF>2.0.CO;2)
- 694 Iida, Y., Takatani, Y., Kojima, A., and Ishii, M.: Global trends of ocean CO₂ sink and ocean acidifica-
695 tion: an observation-based reconstruction of surface ocean inorganic carbon variables, *J.
696 Oceanogr.*, 77, 323-358, <https://doi.org/10.1007/s10872-020-00571-5>, 2021.
- 697 Jiang, F., Wang, H., Chen, J. M., Ju, W., Tian, X., Feng, S., Li, G., Chen, Z., Zhang, S., Lu, X., Liu, J.,
698 Wang, H., Wang, J., He, W., and Wu, M.: Regional CO₂ fluxes from 2010 to 2015 inferred from
699 GOSAT XCO₂ retrievals using a new version of the Global Carbon Assimilation System, *Atmos.
700 Chem. Phys.*, 21, 1963–1985, <https://doi.org/10.5194/acp-21-1963-2021>, 2021.
- 701 Jiang, F., Ju, W., He, W., Wu, M., Wang, H., Wang, J., Jia, M., Feng, S., Zhang, L., and Chen, J. M.: A
702 10-year global monthly averaged terrestrial net ecosystem exchange dataset inferred from the
703 ACOS GOSAT v9 XCO₂ retrievals (GCAS2021), *Earth Syst. Sci. Data*, 14, 3013–3037,
704 <https://doi.org/10.5194/essd-14-3013-2022>, 2022.
- 705 Jin, J., Lin, H. X., Heemink, A., and Segers, A.: Spatially varying parameter estimation for dust emis-
706 sions using reduced-tangent-linearization 4DVar, *Atmos. Environ.*, 187, 358-373,
707 <https://doi.org/10.1016/j.atmosenv.2018.05.060>, 2018.
- 708 Jones, M. W., Andrew, R. M., Peters, G. P., Janssens-Maenhout, G., De-Gol, A. J., Ciais, P., Patra, P.
709 K., Chevallier, F., and Le Quéré, C.: Gridded fossil CO₂ emissions and related O₂ combustion
710 consistent with national inventories 1959–2018, *Sci. Data*, 8, 2, [https://doi.org/10.1038/s41597-
711 020-00779-6](https://doi.org/10.1038/s41597-020-00779-6), 2021.
- 712 Lauvaux, T., Pannekoucke, O., Sarrat, C., Chevallier, F., Ciais, P., Noilhan, J., and Rayner, P. J.: Struc-
713 ture of the transport uncertainty in mesoscale inversions of CO₂ sources and sinks using ensemble
714 model simulations, *Biogeosciences*, 6, 1089–1102, <https://doi.org/10.5194/bg-6-1089-2009>, 2009.
- 715 Liu, J., Bowman, K. W., Schimel, D. S., Parazoo, N. C., Jiang, Z., Lee, M., Bloom, A. A., Wunch, D.,
716 Frankenberg, C., Sun, Y., O'Dell, C. W., Gurney, K. R., Menemenlis, D., Gierach, M., Crisp, D.,
717 and Eldering, A.: Contrasting carbon cycle responses of the tropical continents to the 2015–2016
718 El Niño, *Science*, 358, eaam5690, <https://doi.org/10.1126/science.aam5690>, 2017.
- 719 Miller, C. E., Crisp, D., DeCola, P. L., Olsen, S. C., Randerson, J. T., Michalak, A. M., Alkhaled, A.,
720 Rayner, P., Jacob, D. J., Suntharalingam, P., Jones, D. B. A., Denning, A. S., Nicholls, M. E.,
721 Doney, S. C., Pawson, S., Boesch, H., Connor, B. J., Fung, I. Y., O'Brien, D., Salawitch, R. J.,
722 Sander, S. P., Sen, B., Tans, P., Toon, G. C., Wennberg, P. O., Wofsy, S. C., Yung, Y. L., and Law,
723 R. M.: Precision requirements for space - based data, *J. Geophys. Res.: Atmos.*, 112,
724 <https://doi.org/10.1029/2006jd007659>, 2007.
- 725 Miller, S. M., Michalak, A. M., Yadav, V., and Tadić, J. M.: Characterizing biospheric carbon balance
726 using CO₂ observations from the OCO-2 satellite, *Atmos. Chem. Phys.*, 18, 6785–6799,

- 727 <https://doi.org/10.5194/acp-18-6785-2018>, 2018.
- 728 Miyazaki, K., Eskes, H. J., Sudo, K., Takigawa, M., van Weele, M., and Boersma, K. F.: Simultaneous
729 assimilation of satellite NO₂, O₃, CO, and HNO₃ data for the analysis of tropospheric chemical
730 composition and emissions, *Atmos. Chem. Phys.*, 12, 9545–9579, [https://doi.org/10.5194/acp-12-](https://doi.org/10.5194/acp-12-9545-2012)
731 9545-2012, 2012.
- 732 ObsPack: Cooperative Global Atmospheric Data Integration Project: Multi-laboratory compilation of
733 atmospheric carbon dioxide data for the period 1957-2022; `obspack_co2_1_GLOBALVIEW-`
734 `plus_v9.1_2023-12-08`; NOAA Earth System Research Laboratory, Global Monitoring Labora-
735 tory, <http://doi.org/10.25925/20231201>, 2023.
- 736 Palmer, P. I., Feng, L., Baker, D., Chevallier, F., Bösch, H., and Somkuti, P.: Net carbon emissions
737 from African biosphere dominate pan-tropical atmospheric CO₂ signal, *Nat. Commun.*, 10, 3344,
738 <http://doi.org/10.1038/s41467-019-11097-w>, 2019.
- 739 Peiro, H., Crowell, S., Schuh, A., Baker, D. F., O'Dell, C., Jacobson, A. R., Chevallier, F., Liu, J.,
740 Eldering, A., Crisp, D., Deng, F., Weir, B., Basu, S., Johnson, M. S., Philip, S., and Baker, I.: Four
741 years of global carbon cycle observed from the Orbiting Carbon Observatory 2 (OCO-2) version
742 9 and in situ data and comparison to OCO-2 version 7, *Atmos. Chem. Phys.*, 22, 1097–1130,
743 <https://doi.org/10.5194/acp-22-1097-2022>, 2022.
- 744 Peters, W., Jacobson, A. R., Sweeney, C., Andrews, A. E., Conway, T. J., Masarie, K., Miller, J. B.,
745 Bruhwiler, L. M. P., Pétron, G., Hirsch, A. I., Worthy, D. E. J., van der Werf, G. R., Randerson, J.
746 T., Wennberg, P. O., Krol, M. C., and Tans, P. P.: An atmospheric perspective on North American
747 carbon dioxide exchange: CarbonTracker, *P. Natl. Acad. Sci. USA*, 104, 1892518930,
748 <https://doi.org/10.1073/pnas.0708986104>, 2007.
- 749 Peylin, P., Law, R. M., Gurney, K. R., Chevallier, F., Jacobson, A. R., Maki, T., Niwa, Y., Patra, P. K.,
750 Peters, W., Rayner, P. J., Rödenbeck, C., van der Laan-Luijkx, I. T., and Zhang, X.: Global atmos-
751 pheric carbon budget: results from an ensemble of atmospheric CO₂ inversions, *Biogeosciences*,
752 10, 6699–6720, <https://doi.org/10.5194/bg-10-6699-2013>, 2013.
- 753 Philip, S., Johnson, M. S., Baker, D. F., Basu, S., Tiwari, Y. K., Indira, N. K., Ramonet, M., and Poulter,
754 B.: OCO-2 Satellite-Imposed Constraints on Terrestrial Biospheric CO₂ Fluxes Over South Asia,
755 *J. Geophys. Res.: Atmos.*, 127, e2021JD035035, <https://doi.org/10.1029/2021JD035035>, 2022.
- 756 Piao, S., Wang, X., Wang, K., Li, X., Bastos, A., Canadell, J. G., Ciais, P., Friedlingstein, P., and Sitch,
757 S.: Interannual variation of terrestrial carbon cycle: Issues and perspectives, *Global Change Biol.*,
758 26, 300-318, <https://doi.org/10.1111/gcb.14884>, 2020.
- 759 Randerson, J. T., Van Der Werf, G. R., Giglio, L., Collatz, G. J., and Kasibhatla, P. S.: Global Fire
760 Emissions Database, Version 4.1 (GFEDv4), <https://doi.org/10.3334/ORNLDAAAC/1293>, 2017.
- 761 Takahashi, T., Sutherland, S. C., Wanninkhof, R., Sweeney, C., Feely, R. A., Chipman, D. W., Hales,
762 B., Friederich, G., Chavez, F., Sabine, C., Watson, A., Bakker, D. C. E., Schuster, U., Metzl, N.,
763 Yoshikawa-Inoue, H., Ishii, M., Midorikawa, T., Nojiri, Y., Körtzinger, A., Steinhoff, T., Hoppema,

- 764 M., Olafsson, J., Arnarson, T. S., Tilbrook, B., Johannessen, T., Olsen, A., Bellerby, R., Wong, C.
765 S., Delille, B., Bates, N. R., and de Baar, H. J. W.: Climatological mean and decadal change in
766 surface ocean pCO₂, and net sea-air CO₂ flux over the global oceans, *Deep Sea Res. Pt. II*, 56,
767 554–577, <https://doi.org/10.1016/j.dsr2.2008.12.009>, 2009.
- 768 Taylor, T. E., O'Dell, C. W., Baker, D., Bruegge, C., Chang, A., Chapsky, L., Chatterjee, A., Cheng, C.,
769 Chevallier, F., Crisp, D., Dang, L., Drouin, B., Eldering, A., Feng, L., Fisher, B., Fu, D., Gunson,
770 M., Haemmerle, V., Keller, G. R., Kiel, M., Kuai, L., Kurosu, T., Lambert, A., Laughner, J., Lee,
771 R., Liu, J., Mandrake, L., Marchetti, Y., McGarragh, G., Merrelli, A., Nelson, R. R., Osterman,
772 G., Oyafuso, F., Palmer, P. I., Payne, V. H., Rosenberg, R., Somkuti, P., Spiers, G., To, C., Weir,
773 B., Wennberg, P. O., Yu, S., and Zong, J.: Evaluating the consistency between OCO-2 and OCO-
774 3 XCO₂ estimates derived from the NASA ACOS version 10 retrieval algorithm, *Atmos. Meas.*
775 *Tech.*, 16, 3173–3209, <https://doi.org/10.5194/amt-16-3173-2023>, 2023.
- 776 Thompson, R. L., Patra, P. K., Chevallier, F., Maksyutov, S., Law, R. M., Ziehn, T., van der Laan-
777 Luijkx, I. T., Peters, W., Ganshin, A., Zhuravlev, R., Maki, T., Nakamura, T., Shirai, T., Ishizawa,
778 M., Saeki, T., Machida, T., Poulter, B., Canadell, J. G., and Ciais, P.: Top-down assessment of the
779 Asian carbon budget since the mid1990s, *Nat. Commun.*, 7, 10724,
780 <https://doi.org/10.1038/ncomms10724>, 2016.
- 781 Tilmes, S.: GEOS5 Global Atmosphere Forcing Data, Research Data Archive at the National Center
782 for Atmospheric Research, Computational and Information Systems Laboratory [dataset],
783 <https://doi.org/10.5065/QTSA-G775>, 2016.
- 784 Wang, H., Jiang, F., Wang, J., Ju, W., and Chen, J. M.: Terrestrial ecosystem carbon flux estimated
785 using GOSAT and OCO-2 XCO₂ retrievals, *Atmos. Chem. Phys.*, 19, 12067–12082,
786 <https://doi.org/10.5194/acp-19-12067-2019>, 2019.
- 787 Wang, H., Jiang, F., Liu, Y., Yang, D., Wu, M., He, W., Wang, J., Wang, J., Ju, W., and Chen, J. M.:
788 Global Terrestrial Ecosystem Carbon Flux Inferred from TanSat XCO₂ Retrievals, *J. Remote*
789 *Sens.*, 2022, <https://doi.org/10.34133/2022/9816536>, 2022.
- 790 Whitaker, J. S. and Hamill, T. M.: Ensemble Data Assimilation without Perturbed Observations, *Mon.*
791 *Weather Rev.*, 130, 1913-1924, [https://doi.org/10.1175/1520-0493\(2002\)130<1913:ED-](https://doi.org/10.1175/1520-0493(2002)130<1913:ED-)
792 [AWPO>2.0.CO;2](https://doi.org/10.1175/1520-0493(2002)130<1913:ED-AWPO>2.0.CO;2), 2002.
- 793 Zhang, S., Zheng, X., Chen, J. M., Chen, Z., Dan, B., Yi, X., Wang, L., and Wu, G.: A gl
794 obal carbon assimilation system using a modified ensemble Kalman filter, *Geosci. Model*
795 *Dev.*, 8, 805-816, <https://doi.org/10.5194/gmd-8-805-2015>, 2015.